



CHALMERS
UNIVERSITY OF TECHNOLOGY

Unraveling the ground-state structure of BaZrO₃ by neutron scattering experiments and first-principle calculations

Downloaded from: <https://research.chalmers.se>, 2021-08-31 11:04 UTC

Citation for the original published paper (version of record):

Perrichon, A., Jedvik Granhed, E., Romanelli, G. et al (2020)

Unraveling the ground-state structure of BaZrO₃ by neutron scattering experiments and first-principle calculations

Chemistry of Materials, 32(7): 2824-2835

<http://dx.doi.org/10.1021/acs.chemmater.9b04437>

N.B. When citing this work, cite the original published paper.

Unraveling the Ground-State Structure of BaZrO₃ by Neutron Scattering Experiments and First-Principles Calculations

Adrien Perrichon, Erik Jedvik Granhed, Giovanni Romanelli, Andrea Piovano, Anders Lindman, Per Hyldgaard, Göran Wahnström,* and Maths Karlsson*



Cite This: *Chem. Mater.* 2020, 32, 2824–2835



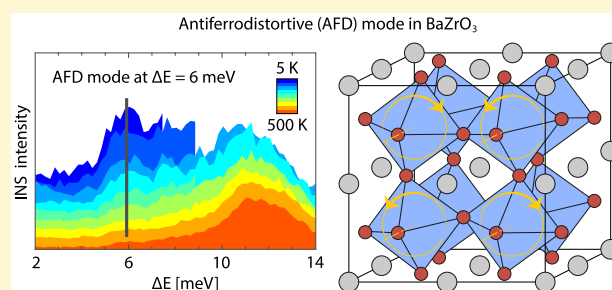
Read Online

ACCESS |

Metrics & More

Article Recommendations

ABSTRACT: The all-inorganic perovskite barium zirconate, BaZrO₃, is a widely used material in a range of different technological applications. However, fundamental questions surrounding the crystal structure of BaZrO₃, especially in regard to its ground-state structure, remain. While diffraction techniques indicate a cubic structure all the way down to $T = 0$ K, several first-principles phonon calculation studies based on density functional theory indicate an imaginary (unstable) phonon mode due to the appearance of an antiferrodistortive transition associated with rigid rotations of ZrO₆ octahedra. The first-principles calculations are highly sensitive to the choice of exchange-correlation functional and, using six well-established functional approximations, we show that a correct description about the ground-state structure of BaZrO₃ requires the use of hybrid functionals. The ground-state structure of BaZrO₃ is found to be cubic, which is corroborated by experimental results obtained from neutron powder diffraction, inelastic neutron scattering, and neutron Compton scattering experiments.



each other and thereby facilitate the transfer.^{1,13–16} The flexibility and motion of the oxygen sublattice becomes important.

1. INTRODUCTION

Perovskite-type oxides, of the general chemical formula ABO₃, where A and B denote different metal ions, constitute an extremely important class of materials, with properties such as electronic and/or ionic conductivity,¹ multiferroicity,² piezoelectricity,³ magnetocalorimetry,⁴ and luminescence.⁵ These properties make them highly attractive for a range of technological applications. Various cation substitutions and/or variation of the temperature are common means to alter the properties of the perovskites, but their underlying mechanisms are, in several cases, unclear. In particular, the closeness in energy between the various temperature-dependent phases represents a formidable challenge, both for experiments and for a theoretical description.

Barium zirconate (BaZrO₃) based ceramic materials have recently gained considerable attention for applications in protonic fuel cell applications^{6–10} and hydrogen separation membranes.^{11,12} Protons are introduced into the perovskite lattice by a process involving acceptor-doping to the Zr site, followed by hydration in a humid atmosphere at which the protons form covalent bonds with the oxygen ions of the perovskite lattice.¹ The basic mechanism for the proton mobility consists of rotational diffusion of the protonic defect (–OH) around the oxide ion and a proton transfer to a neighboring oxide ion. The proton transfer is generally believed to be the rate limiting process and is driven by a bending type motion whereby two oxygen ions come close to

Fundamental questions surrounding the crystal structure of BaZrO₃, especially in regard to its ground-state structure, remain. Also in this case, the motion of the oxygen sublattice becomes important. While diffraction techniques indicate a cubic structure all the way down to $T = 0$ K, several first-principles phonon calculation studies indicate an imaginary (unstable) phonon mode due to the appearance of an antiferrodistortive (AFD) transition associated with rigid rotations of the ZrO₆ oxygen octahedra corresponding to out-of-phase tilts of sequential octahedra. An accurate description of, in particular, the oxygen sublattice motion therefore becomes critical for both establishing the ground-state structure of BaZrO₃ and for modeling the proton mobility in acceptor-doped BaZrO₃. Here, we will scrutinize the ground-state structure of BaZrO₃, both experimentally and theoretically.

Received: October 29, 2019
Revised: March 13, 2020
Published: March 24, 2020



The high-symmetry structure of ABO_3 perovskites is simple cubic, with the O ions at the face centers, the A ion at the cube corners, and the B ion in the body center (Figure 1a). The

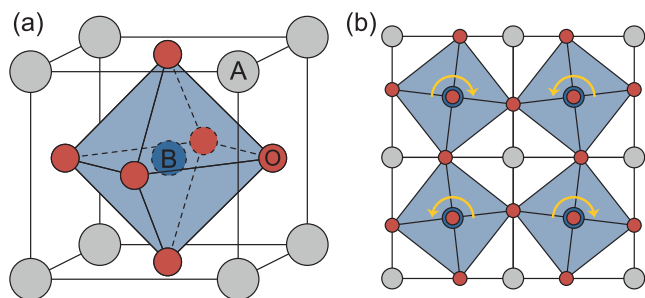


Figure 1. Schematic representation of the ABO_3 perovskite in its high-symmetry cubic structure (a) and upon an AFD phase transition (b). The yellow arrows represent the displacements from the high-symmetry cubic structure. The A, B, and O atoms are represented by gray, blue, and red spheres, respectively.

cubic structure is common at sufficiently high temperatures, while upon lowering of the temperature the ABO_3 perovskites generally display a number of structural phase transitions to phases of lower symmetry. The $BaZrO_3$ perovskite may be a very rare exception that stays cubic all the way down to $T = 0$ K. A very common transition is the out-of-phase AFD transition (Figure 1b) which is manifested in theoretical spectra as the appearance of an imaginary (unstable) phonon mode at the R-point of the Brillouin zone of the cubic perovskite structure, and in the experimental spectra as, so-called, soft modes. The AFD instability is found to be well correlated with the Goldschmidt tolerance factor, $t = (r_A + r_O) / \sqrt{2}(r_B + r_O)$, where r_A , r_B , and r_O are the ionic radii for the A, B, and O species, respectively. For $t = 1$, there is a perfect match to a cubic lattice in which rigid spheres with radii of the corresponding ions are perfectly stuck together. For $t < 1$, the A cation is small as compared with the cage of the surrounding oxygen ions and rigid rotations of the BO_6 octahedra commonly occur to optimize the A–O bond distances. For example, $CaTiO_3$ with $t = 0.97$ ¹⁷ remains cubic down to about $T = 1523$ K where it makes an AFD transition to a tetragonal structure,¹⁸ whereas $SrTiO_3$, with a nearly optimal tolerance factor of $t = 1.01$,¹⁷ remains cubic down to $T = 110$ K.¹⁹

Barium zirconate, $BaZrO_3$, also with a nearly optimal tolerance factor of $t = 1.01$ ¹⁷ is a prominent candidate perovskite to stay cubic down to $T = 0$ K. Experimentally, both X-ray and neutron powder diffraction (XRPD and NPD, respectively) data, indeed suggest a cubic structure down to, at least, $T = 2$ K.²⁰ Theoretically, however, first-principles calculations based on density functional theory (DFT) show varying results, highly sensitive to the choice of exchange-correlation (XC) functional in the calculations. Specifically, the use of the local density approximation (LDA)^{20–23} and the PW91,²⁴ PBEsol²⁵ and Wu–Cohen²⁶ functionals predicts an instability at the R-point of the Brillouin zone, thus pointing toward an AFD transition, whereas the use of PBE,²⁷ RPBE,²⁷ and PBE0²⁸ functionals predicts a stable cubic structure at low temperature.

In cases where the instability, as observed in the DFT calculations, is weak, it has been suggested that quantum fluctuations may suppress the phase transition in $BaZrO_3$ and the material therefore stays cubic all the way down to $T = 0$

K.^{20,21,24,25} Such quantum fluctuations have been shown to completely suppress the predicted ferroelectric (FE) transition in $SrTiO_3$.²⁹ However, it has been argued that they are not sufficient in $BaZrO_3$ to suppress the transition. Instead, due to the closeness of the energies of the phases allowed from condensation of the R mode, a structural “glass state” may be formed upon cooling and the system would appear cubic on average.²³ A somewhat similar idea, an “inherent dynamical disorder”, has been put forward to account for the apparent local deviation from a cubic structure identified by Raman spectroscopy of $BaZrO_3$ powder.³⁰ It is suggested that correlated tilts of ZrO_6 octahedra may occur on a local length-scale, shorter than what is probed by conventional diffraction methods where only the average cubic structure is observed. However, recent Raman studies on a single-crystal sample of $BaZrO_3$ show no direct evidence for such “nanodomains”, and the spectra are instead explained by classical second-order Raman scattering.³¹ In fact, as our knowledge about the real ground-state structure of $BaZrO_3$ has advanced, it has become clear that this seemingly simple material is a very challenging one. It is only through a more systematic, combined experimental and theoretical study that a clear mechanistic picture of the ground-state structure of $BaZrO_3$ will emerge.

Here, we present a systematic analysis of the temperature dependence of the structure and dynamics of $BaZrO_3$, using a combination of high-resolution NPD, inelastic neutron scattering (INS), neutron Compton scattering (NCS), and first-principles DFT calculations. NPD gives information on the average structure but also the displacements of the nuclei from their equilibrium positions through the atomic displacement parameters (ADPs). The INS measurements are used to probe the vibrational properties of the powder sample for wave vectors close the R-point of the Brillouin zone, as a function of temperature, and NCS provides direct access to the nuclear momentum distributions. The quantal and thermal fluctuations of the ionic positions are therefore obtained as a function of temperature both in momentum space, through the NCS measurements, and in ordinary space, through the extraction of the ADPs from the NPD measurements. Six different well-established XC functional approximations are used in the DFT calculations to carefully investigate the accuracy of the theoretical predictions and, together with the experimental studies, establish the structure of $BaZrO_3$.

2. EXPERIMENTAL TECHNIQUES

2.1. Neutron Powder Diffraction. The NPD experiment was performed at the high-resolution two-axis diffractometer D2B at the Institut Laue Langevin (ILL), France. Data were collected on 6.3 g of polycrystalline $BaZrO_3$ powder, placed in a cylindrical sample holder of Al with a diameter of 8 mm inside a standard cryostat. The wavelength was set to $\lambda = 1.051$ Å using the (557) reflection of a vertically focusing germanium monochromator. Diffractograms were collected at $T = 5, 100,$ and 300 K. The data were analyzed using the standard Rietveld refinement method as implemented in the FullProf software.³²

2.2. Inelastic Neutron Scattering. The INS experiment was performed on the thermal neutron three-axis spectrometer IN8 at the ILL, France. The sample, the same as used in the NPD experiment, was placed in an open cylindrical sample holder of Nb—a purely coherent scatterer, chosen to minimize the incoherent contribution of the elastic line. The measurements were performed at a constant neutron final energy, $E_f = 14.68$ meV (corresponding to a final neutron wave vector of $k_f = 2.662$ Å⁻¹), using as focusing monochromator the (111) reflection of doubly bent Si single crystals

and as analyzer the (200) reflection of Cu single crystals. This setup was associated with an energy resolution of 0.57 meV at the elastic line, and a momentum transfer (Q) resolution of 0.03 \AA^{-1} . A pyrolytic graphite filter was used to suppress the third-order harmonics from the Si monochromator crystals.

While the IN8 spectrometer may be used to measure phonon dispersions of single-crystal samples, it is used here to specifically measure the phonon modes at the Q -values corresponding to the R-points of the Brillouin zone, since all the directions are merged in a powder sample. We thus measured spectra at constant Q , referred to as ω -scans, at the Q -point (1.5 1.5 1.5), corresponding to $|Q| \approx 2.9 \text{ \AA}^{-1}$. Measurements of the other accessible R-points were inconclusive, as the spectrum at (0.5 0.5 0.5) was contaminated by spurious signals and the spectra at (1.5 0.5 0.5) and (1.5 1.5 0.5) contain overlapping contributions from other high-symmetry points of the Brillouin zone. Spectra were collected between $T = 5$ and $T = 500$ K using a cryofurnace.

2.3. Neutron Compton Scattering. The NCS experiment was performed at the ISIS Pulsed Neutron and Muon Source in the U.K. on the VESUVIO spectrometer.³³ VESUVIO is an inverted-geometry spectrometer where the final energy of scattered neutrons is fixed to 4.9 eV by a nuclear resonance of a Au foil³⁴ and the incident energy is obtained by time-of-flight measurements. The sample, 14.15 g of BaZrO₃ powder, was loaded into a Sn sachet of the cross-sectional area $3 \text{ cm} \times 3 \text{ cm}$. NCS spectra were measured at $T = 15$ and $T = 300$ K using the VESUVIO backscattering detector banks, in the scattering-angle range between 130° and 170° and sample–detector distances between 0.4 m and 0.6 m. The temperature was controlled using a closed circuit refrigerator.

The formalism of NCS has been recently reviewed in ref 35. Importantly, as the energy transfer $\hbar\omega$ and the momentum transfer Q are in the range 1–800 eV and 30 – 200 \AA^{-1} , respectively, the scattering process can be described within the impulse approximation.³⁶ By imposing the conservation of the total kinetic energy and momentum in the neutron-plus-atom system, it follows that the dynamical structure factor, $S(\mathbf{Q}, \hbar\omega)$, simplifies to a linear superposition of contributions from each isotope of mass M in the sample, $S_M(\mathbf{Q}, \hbar\omega)$, centered along the recoil lines $\hbar\omega = \hbar^2 Q^2 / 2M$. Each function $S_M(\mathbf{Q}, \hbar\omega)$ is defined from the distribution of momenta \mathbf{p} of the scattering atom of mass M in the direction of the momentum transfer $\hat{\mathbf{Q}}$

$$\frac{\hbar Q}{M} S_M(\hat{\mathbf{Q}}, \hbar\omega) = J(y_M; \hat{\mathbf{Q}}) = \hbar \int n(\mathbf{p}) \delta(\hbar y - \mathbf{p} \cdot \hat{\mathbf{Q}}) d\mathbf{p} \quad (1)$$

where $n(\mathbf{p})$ is the momentum distribution, $y_M = (M/\hbar^2 Q)[\hbar\omega - \hbar^2 Q^2 / 2M]$, and $J(y_M; \hat{\mathbf{Q}})$ is the so-called neutron Compton profile (NCP).³⁵ For a powder sample, such as the one studied here, the momentum distribution $n(\mathbf{p})$ can be measured as a function of the magnitude of \mathbf{p} only, and the directional information on $\hat{\mathbf{Q}}$ is lost. Moreover, in the approximation of an isotropic and harmonic potential, the NCP can be written as a normalized Gaussian of the form

$$J(y_M) = \frac{1}{\sqrt{2\pi\sigma_M^2}} \exp\left(-\frac{y_M^2}{2\sigma_M^2}\right) \quad (2)$$

where σ_M is the standard deviation of the momentum distribution of mass M . From the measurement of σ_M it is possible to define the mean kinetic energy of the atom of mass M as $\langle E_{\text{kin}} \rangle = 3\hbar^2 \sigma_M^2 / 2M$. One should notice that the powder-averaged NCP can still provide information on the anisotropy of the local potential, as in the case of deuterium and oxygen NCPs in heavy water,³⁷ because the powder-average of an anisotropic NCP corresponds to a Gauss–Hermite expansion rather than a simple Gaussian function.³⁸ In general, the standard deviations of the momentum and spatial distributions are related to each other via the Heisenberg uncertainty principle. Therefore, a direct measurement of σ_M allows an estimate of the spatial delocalization of an atom of the order of $1/2\sigma_M$.

3. FIRST-PRINCIPLES CALCULATIONS

The first-principles DFT calculations were performed using the projector augmented wave (PAW) method^{39,40} as implemented in the VASP^{41,42} software. Six different approximations to the XC functional were used. The LDA and the two constraint-based semilocal generalized gradient approximations (GGAs), PBE⁴³ and PBEsol,⁴⁴ where the latter is specifically designed for solids, were also used. The consistent-exchange vdW-DF-cx functional,^{45–47} henceforth abbreviated as CX, is a version of the van der Waals density functional method.^{47–49} It captures truly nonlocal correlations and balances exchange and correlation by use of the Lindhard screening logic.⁴⁸

A fraction of Fock exchange is included in two hybrid functionals. The vdW-DF-cx0p,⁵⁰ henceforth abbreviated as CX0p, is a hybrid extension of the CX functional⁵¹ and includes both nonlocal correlations and nonlocal Fock exchange. The fraction of Fock exchange is set at 20%, following a coupling constant scaling analysis⁵² of binding in sparse matter.⁵⁰ HSE^{53,54} (sometimes called HSE06) is a range-separated hybrid extension of the PBE functional using 25% Fock exchange for the description of the short-range Coulomb interaction. The range separation is described by a screening parameter $\mu = 0.2 \text{ \AA}^{-1}$ in an error-function weighting $\text{erf}(\mu r)/r$ of the Coulomb interaction.⁵³

Convergence of the R mode turned out to be very sensitive to the oxygen PAW potential and the energy cutoff. VASP comes with several different PAW potentials for oxygen. Both the regular and the hard PAW potentials treat $2s^2 2p^4$ as valence states but with different core radii. The standard PAW potential for oxygen has core radii $r_s = 0.635$, $r_{p,d} = 0.804$, and a nominal energy cutoff of 400 eV, while the hard has $r_{s,p,d} = 0.582$ and 700 eV, respectively. For the LDA, the regular PAW potential for oxygen was used with an energy cutoff of 900 eV. The semilocal functionals PBE and PBEsol were treated using hard PAW potentials and an energy cutoff of 1200 eV, while for the functionals including nonlocal Fock-exchange and/or nonlocal correlation, CX, and the hybrids HSE and CX0p, hard PAW potentials and energy cutoffs of 1600 eV were required for full convergence. Convergence turned out to be less sensitive to the k -point sampling and a $6 \times 6 \times 6$ k -point mesh was deemed sufficient for the hybrid functionals, while $8 \times 8 \times 8$ was used for all nonhybrids.

The phonon spectra were calculated using the frozen phonon method with the default displacement of 0.01 \AA in $2 \times 2 \times 2$ supercells containing 40 atoms and postprocessed in phonopy.⁵⁵ A $10 \times 10 \times 10$ k -point mesh was used for sampling of the Brillouin zone for all phonon calculations. In order to compare to the experimental INS spectra, the theoretical neutron scattering cross sections for a powder sample of BaZrO₃ was derived, using the *in-house* PowderTAS code.⁵⁶ The theoretical spectra were obtained by powder-averaging of the coherent and incoherent, elastic, and one-phonon emission cross sections, using phonon eigenvectors and eigenvalues from DFT based phonon calculations. The PowderTAS code performs, for a series of Q -values, the powder-average of the neutron scattering cross sections calculated for a large number of randomly oriented Q -vectors, hence forming a $S(Q, \hbar\omega)$ scattering map.

4. RESULTS AND DISCUSSION

4.1. Neutron Powder Diffraction Measurements. The NPD data of BaZrO₃ (Figure 2) show that the material is

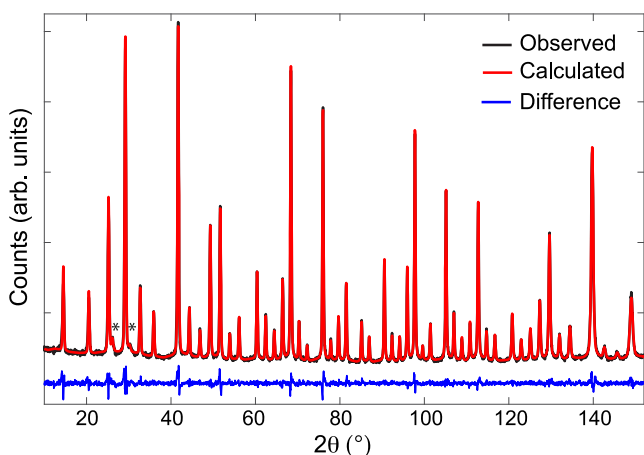


Figure 2. NPD data for BaZrO₃ at $T = 5$ K (black), calculated diffraction pattern by the Rietveld method (red), and difference line (blue). The small peaks marked with asterisks are the Al (111) and (200) Bragg peaks from the sample environment.

monophasic and can be indexed in the cubic $Pm\bar{3}m$ space group at all three measured temperatures, $T = 5, 100,$ and 300 K, in accordance with the results from previous NPD experiments.²⁰ The corresponding parameters from the Rietveld refinement are reported in Table 1. We note, however, that the refined occupancy factors correspond to a deviation from the BaZrO₃ stoichiometry, an excess of BaO or equivalently, a loss of ZrO₂ (Table 1). The lack of superstructure and secondary phase peaks indicates that deviation from the BaZrO₃ stoichiometry is accommodated by randomly distributed defects, which is consistent with the pronounced Lorentzian component of the peak shape (cf. Y in Table 1), which generally indicates a reduced size of the scattering domains.

The anisotropic ADPs are shown as mean-square displacement tensors with terms reported in Table 1 as $\langle u_{\alpha\beta}^2 \rangle$, where α and β correspond to Cartesian direction indexes. We observe

that both Ba and Zr show isotropic ADPs, where the one for Ba is somewhat larger in magnitude. The O displacements are highly anisotropic, corresponding to an oblate ellipsoid, and the corresponding ADPs are considerably larger. Note that the ADPs also contain contributions, if any, of small static distortions, which may lead to its value being slightly overestimated with respect to the real mean-square displacement of the atoms.

4.2. Structure and Vibrations. Table 2 shows the equilibrium lattice constants for the six different XC functional approximations, as determined from the DFT calculations. The lattice constants range from the well-known underestimation in LDA to the likewise well-known overestimation of PBE, with about $\pm 1\%$, respectively. The CX and PBEsol functionals, as well as the two hybrid functionals HSE and CX0p, predict values between the extremes and agree well with the experimental value.

The stability of the cubic phase can be investigated by determining the phonon dispersion curves. The result using phonopy⁵⁵ is shown in Figure 3, with the inset showing a closeup around the R-point. The three functionals LDA, PBEsol, and CX all show an AFD R-mode instability while PBE and the two hybrid functionals predict a stable cubic structure. This unstable phonon mode, associated with the octahedral rotation motion, is hereafter denoted R_{25} . The corresponding frequencies are given in Table 2. The results using the hybrid functionals give a frequency 2–3 times larger compared with PBE.

The stability of the cubic phase can be further investigated by mapping out the potential energy surface of the AFD mode. A potential energy surface can be generated by displacing the oxygen atoms along the R_{25} phonon eigenmode while keeping the lattice spacing constant. The surface generated in this fashion can be well described by the expression^{21,25,57}

$$E = \frac{1}{2}\kappa u^2 + \alpha u^4 \quad (3)$$

Table 1. Crystallographic Parameters from the Rietveld Refinement of the NPD Data at $T = 5, 100,$ and 300 K in the $Pm\bar{3}m$ Space Group^a

		temperature		
		$T = 5$ K	$T = 100$ K	$T = 300$ K
Lattice parameters	a (Å)	4.18763(3)	4.18822(3)	4.19209(4)
	Ba:(1b) (1/2 1/2 1/2)	$\langle u_{11}^2 \rangle$ (Å ² × 10 ⁻⁴)	18(2)	28(2)
	Occ.: fixed	1	1	1
Zr:(1a) (0 0 0)	$\langle u_{11}^2 \rangle$ (Å ² × 10 ⁻⁴)	12(2)	12(2)	33(2)
	Occ.	0.94(1)	0.94(1)	0.94(1)
O:(3d) (1/2 0 0)	$\langle u_{11}^2 \rangle$ (Å ² × 10 ⁻⁴)	21(3)	23(3)	45(3)
	$\langle u_{22}^2 \rangle$ (Å ² × 10 ⁻⁴)	58(2)	67(2)	124(2)
	Occ.	2.87(2)	2.88(2)	2.87(2)
Peak shape	X : fixed	0	0	0
	Y	0.097(2)	0.112(2)	0.113(2)
Reliability factors	R_{Bragg}	1.20	1.27	1.21
	R_{wp}	4.91	4.68	4.47
	R_{p}	3.74	3.54	3.41
	χ^2	2.58	2.36	2.19

^aBragg peaks are modelled with Thompson–Cox–Hastings pseudo-Voigt functions that include axial divergence and are parameterized by the peak shape Gaussian (X) and Lorentzian (Y) components. The Al peaks (secondary phase) are processed with a Le Bail refinement. The atomic positions are fixed according to the high-symmetry cubic structure and are indicated in Wyckoff notations and reciprocal lattice units. The occupation (Occ.) of the barium atoms is fixed to reflect the theoretical stoichiometry. The reliability factors of the Rietveld method, R_{Bragg} , R_{wp} , R_{p} , and χ^2 are also reported.

Table 2. Calculated Lattice Constant a_0 , ZPE Corrected Lattice Constant a_0^{ZPE} , Stiffness Parameter κ , and Anharmonicity Coefficient α (See Equation 3), and R_{25} Phonon Mode Frequencies, $\hbar\omega$ and $\hbar\omega^{\text{ZPE}}$, at the Equilibrium Lattice Constant and the ZPE Corrected Lattice Constant, Respectively, for the Six XC Functional Approximations Used in This Work^a

XC	a_0 (Å)	a_0^{ZPE} (Å)	κ (eV/Å ²)	α (eV/Å ⁴)	$\hbar\omega$ (meV)	$\hbar\omega^{\text{ZPE}}$ (meV)
PBE	4.237	4.244	0.040	4.21	2.30	3.39
CX	4.200		−0.054	4.67	2.66i	
PBEsol	4.192		−0.222	5.07	5.38i	
LDA	4.160		−0.394	5.19	7.17i	
HSE	4.202	4.208	0.298	4.64	6.24	6.58
CX0p	4.183	4.188	0.231	4.42	5.49	5.85
exp.	4.188(1)				5.9(2)	

^aThe experimental values for the lattice constant and the R_{25} phonon mode frequency are also indicated (from sections 4.1 and 4.3, respectively).

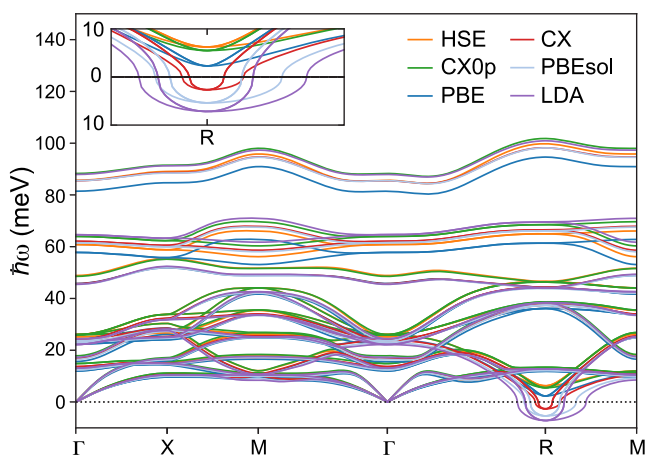


Figure 3. Phonon dispersion computed from DFT using the six different XC functional approximations. (inset) Magnification of the R_{25} phonon mode and its vicinity.

where E is the energy per formula unit (5 atoms) of BaZrO_3 , $u = (a_0/2)\tan\theta$ is the magnitude of the oxygen-atom displacement associated with the rotation of the oxygen octahedra around the [001] axis, and θ is the corresponding tilt angle. The stiffness parameter κ and the anharmonicity coefficient α are then determined through a fit to the computed data. The result is shown in Figure 4 for the different functionals, and the corresponding data for κ and α are given in Table 2. The

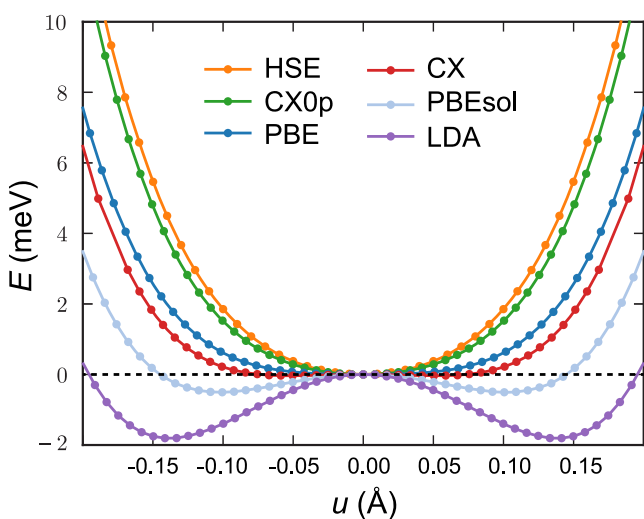


Figure 4. Potential energy surface, per formula unit, mapped out using DFT by displacements along the R_{25} phonon mode.

harmonic frequencies are given by $\hbar\omega = \sqrt{\kappa/M_{\text{eff}}}$, where M_{eff} is the effective mass being displaced. For the R_{25} mode, two oxygen atoms per formula unit are being displaced and hence $M_{\text{eff}} = 2M_{\text{O}}$, where M_{O} is the atomic mass of oxygen.

The existence of minima at finite values for the displacement parameter u indicates a possible phase transition into a tetragonal phase. The PBEsol functional shows a small minimum of -0.44 meV, and CX, a very small minimum of -0.033 meV. It is likely that quantum fluctuations at $T = 0$ K suppress the tetragonal phase transition for these two functionals. Using LDA, a minimum of -1.81 meV is obtained for $u = 0.1381$ Å ($\theta = 3.8^\circ$). By dropping the cubic constraint, the full relaxation leads to the tetragonal $I4/mcm$ phase with $c/a = 1.0031$ and the energy -2.13 meV per formula unit relative to the cubic phase. With regard to the role of quantum fluctuations, previous reports are conflicting in that one report argues that quantum fluctuations are not sufficient to suppress the transition using LDA,²³ whereas other reports state that it is indeed likely that quantum fluctuations will suppress the transition also for LDA.^{20,21} This implies that, most likely, if quantum fluctuations are included, all functionals, maybe with the exception of LDA, will predict a cubic structure down to $T = 0$ K. This is consistent with the experimental finding.

The stiffness parameter κ , which is related to the instability, depends rather strongly on the lattice spacing as can be seen in Figure 5. Consider first the nonhybrid functionals. By comparing these functionals at the experimental lattice

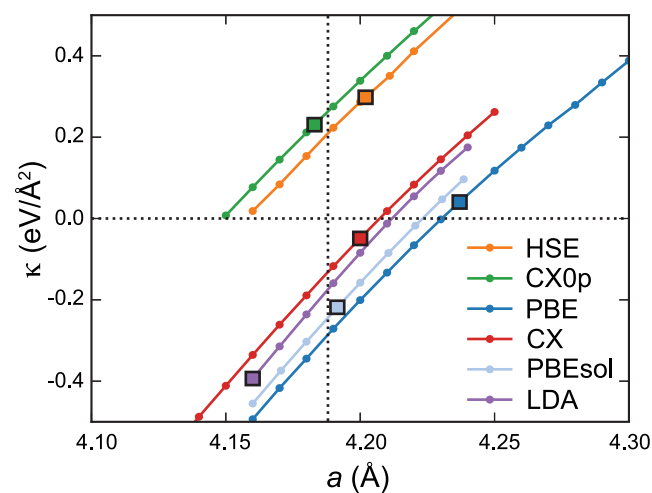


Figure 5. Lattice constant dependence of the stiffness parameter κ for different XC functional approximations. The squares mark the equilibrium lattice constant. The lines serve as guides for the eye.

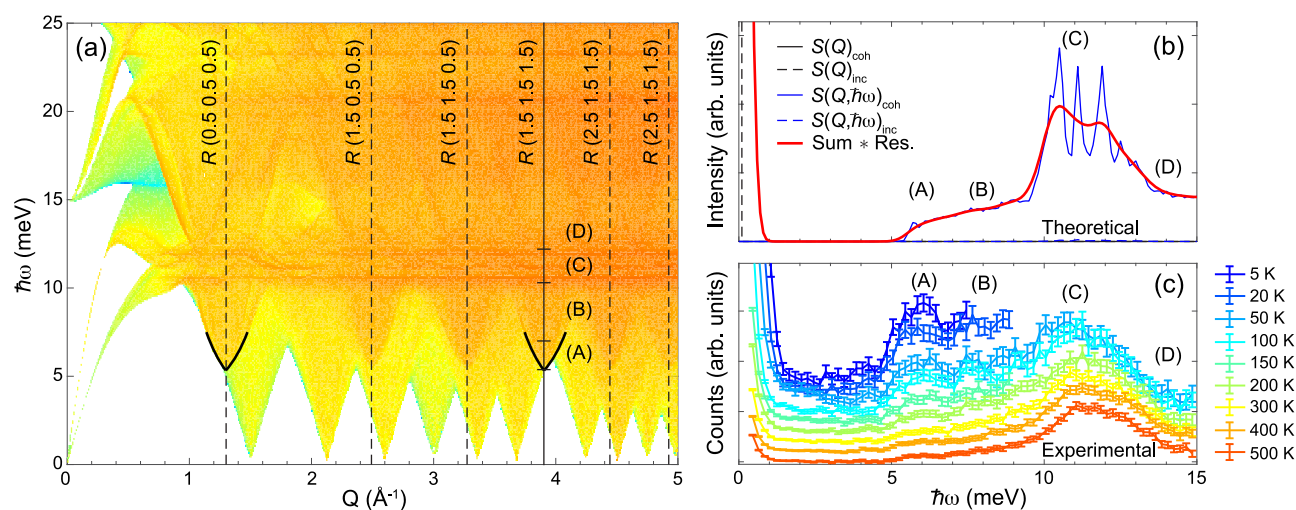


Figure 6. (a) Analytically calculated $(Q, \hbar\omega)$ scattering map of a powder sample of BaZrO_3 , containing the contributions from the coherent and incoherent one-phonon emission cross sections, and coherent and incoherent elastic cross sections, based on the phonon eigenvectors from the CX0p phonon calculation. The color scale represents the predicted scattering intensity, in logarithmic scale. Dashed and full vertical black lines indicate the Q -values associated with the R -points. The minima of the R_{25} phonon mode are outlined around (0.5 0.5 0.5) and (1.5 1.5 1.5). (b) Cut of the calculated scattering map shown in (a) at the (1.5 1.5 1.5) R -point, where the black and blue lines show the elastic and inelastic (one-phonon emission) contributions, respectively. Note that the coherent elastic contribution is zero (not visible) and that the incoherent inelastic contribution is minor (contained within the horizontal axis line). The sum of all four contributions, convoluted to the experimental energy resolution (estimated at 0.57 meV plus 2% of the energy transfer, $\hbar\omega$), is shown in red. (c) Experimental INS data measured at the (1.5 1.5 1.5) R -point as a function of temperature. Spectra are corrected by the zero-shift, by a flat background, and by the Bose population. Spectra are vertically offset for clarity.

constant $a = 4.188 \text{ \AA}$, κ equals -0.174 , -0.244 , -0.131 , and -0.286 eV/\AA^2 for LDA, PBEsol, CX, and PBE, respectively, and PBE now predicts the largest instability. This shows that the main effect of the inclusion of gradient corrections and nonlocal correlation on the R mode stability is secondary and is mostly a consequence of the adjusted lattice constant. For the hybrid functionals, the situation is different. By including the nonlocal Fock exchange the stiffness increases substantially and becomes positive at the experimental lattice constant. The two hybrid functionals behave very similar to each other, and once again, the main difference between the functionals is the different equilibrium lattice spacing. Both functionals increase almost linearly with increasing lattice spacing and with similar magnitude. By reducing the lattice spacing (by applying a pressure) the stiffness parameter κ will also become negative for the hybrid functionals. Indeed, a structural phase transition from the cubic to the tetragonal phase has been observed for BaZrO_3 at about 17 GPa.⁵⁸

For the two hybrid functionals, the ratio between the harmonic and the anharmonic terms in eq 3 is quite small for relevant values of u indicating that for the R_{25} mode anharmonic effects should be relatively small. For the PBE functional the above ratio is considerably larger, and a more pronounced effect from the anharmonicity should be present. To study the anharmonicity and hence the temperature dependence of the R_{25} mode frequency, we make use of the quasi-harmonic approximation.⁵⁵ By taking the lattice expansion due to the zero-point energy (ZPE) fluctuations into account the equilibrium lattice constant is up-shifted by about 0.007 \AA . This shift introduces a slight hardening of the R_{25} mode frequencies. In Table 2 ZPE corrected lattice constants a_0^{ZPE} and corresponding R_{25} mode frequencies $\hbar\omega_{\text{R}}^{\text{ZPE}}$ are given. The temperature dependence is then determined using the quasi-harmonic approximation. For the two hybrid functionals we obtain only a minor increase, about 10% at 500 K (see

Figure 8). For the PBE functional a larger temperature dependence is obtained, consistent with its larger anharmonicity, and at $T = 500 \text{ K}$ the R_{25} mode frequency has increased with about 30%.

4.3. Inelastic Neutron Scattering Measurements.

Figure 6a shows the analytically calculated $(Q, \hbar\omega)$ scattering map of a powder sample of BaZrO_3 , with the Q -values corresponding to the R -point of the Brillouin zone indicated by the vertical dashed lines. We observe that only the (0.5 0.5 0.5) and (1.5 1.5 1.5) R -points are sufficiently separated from other high-symmetry points and Bragg peaks in order for the R_{25} phonon mode to be clearly distinguishable as the lowest-energy inelastic contribution, appearing as an inverted bell-curve with a minimum at about 6 meV. Unfortunately, as the experimental spectra at the (0.5 0.5 0.5) R -point is found to be contaminated by a spurious signal in the energy region of interest, the subsequent analysis concerns the (1.5 1.5 1.5) R -point only (marked with the vertical full line in Figure 6a).

A slice of the scattering map at the (1.5 1.5 1.5) R -point is shown in Figure 6b, detailing the contributions of each cross-section to the calculated scattering intensity, as well as the sum of these contributions convoluted to the experimental resolution. We observe that the elastic intensity is solely due to the incoherent elastic cross-section, and the inelastic spectra to the coherent one-phonon emission cross-section. By comparison between Figure 6a and b, we distinguish four regions of the inelastic spectra. The lowest-energy band (A) is, intensity-wise, mostly due to the R_{25} phonon mode. The scattering intensity progressively increases with energy transfer in region (B) as the relatively weakly intense acoustic phonon branches, from the nearby Bragg peaks (211) and (220), disperse up to a Q -value matching the (1.5 1.5 1.5) R -point. The most intense inelastic contributions (C), constitute the first optic band, appearing as a broad asymmetric band centered at about 11 meV due to resolution effects. A dip in

intensity is observed at higher energy (*D*), in a region where phonon branches are mostly dispersive, in between the 11 and 20 meV nondispersive optic bands.

In Figure 6c, we show the experimental INS spectrum measured by ω -scans at the (1.5 1.5 1.5) R-point, as a function of temperature. It is featured by the incoherent elastic line at $\hbar\omega = 0$ meV, a broad asymmetric band in the range 10–13 meV, and a series of lower-energy bands appearing as shoulders to the optic band, including a relatively well-defined band at about 6 meV. By comparing with the theoretical spectrum in Figure 6b, we identify the 6 meV band to the R_{25} phonon mode (A), and the 10–13 meV band to the first optic band (C).

In order to extract the temperature dependence of the R_{25} phonon mode, we performed a peak fit analysis of the spectra over the energy region 4.7–8.7 meV, using as a fitting model two Gaussian functions corresponding to the bands A and B. The optic band has been omitted to reduce the number of free parameters, as its asymmetry would require up to three Gaussian functions to model, and also to use a single fitting model, as the optic band is not consistently measured in all data sets. Furthermore, the B band is used to model the tail coming from the optic band, with its center fixed at $\hbar\omega = 8.2$ meV and its fwhm fixed to 2.1 meV. Fitted parameters are reported in Figure 7. The integrated intensity of the phonon mode (Figure 7a) decreases exponentially while increasing the temperature, which is consistent with the expected decrease of the intensity due to the Debye–Waller factor. The phonon energy (Figure 7b) and its fwhm (Figure 7c) are found to be

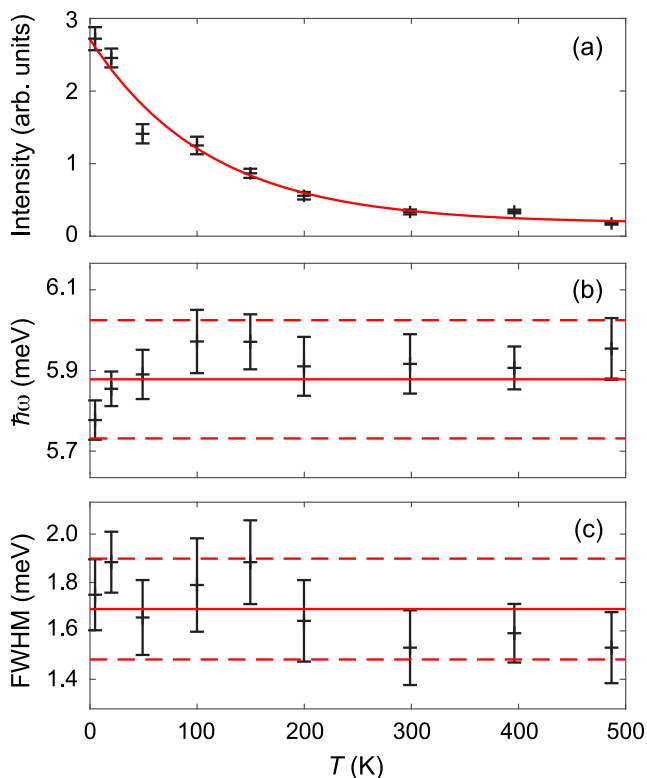


Figure 7. Temperature dependence of the peak fitting parameters obtained from the fitting of the INS spectrum (see text): (a) integrated intensity, (b) vibrational mode energy, and (c) fwhm. Red solid lines represent error-weighted averages or trends (linear regression). Red dashed lines represent the 95% confidence interval.

(within error) temperature independent, with $\hbar\omega = 5.88(15)$ meV and $\text{fwhm} = 1.7(3)$ meV. The large phonon fwhm, compared to the estimated energy resolution of about 0.7 meV at $\hbar\omega = 6$ meV, is rationalized by broadening due to the powder-state of the sample, as it is not a unique phonon line but a bell-shape from the powder-average that is measured (see A in Figure 6a). Furthermore, the phonon line may be broadened due to the presence of defects associated with the sample nonstoichiometry that limits the size of the scattering domains, which would also contribute to the large fwhm. The overall effect of the presence of such defects appears to be limited to finite-size effects of the scattering domains (*Y* parameter in Table 1, possible broadening of the phonon line), and as such should have no significant impact on the stability of the R_{25} phonon. In overall, provided that the 5.9 meV band is indeed the R_{25} phonon, we find it stable down to $T = 5$ K. This would indicate that the presence of a ground-state of lower symmetry than cubic, based on the collapse of the R_{25} phonon mode, is unlikely.

In Figure 8 we compare the calculated and measured temperature dependence of the R_{25} phonon mode. The

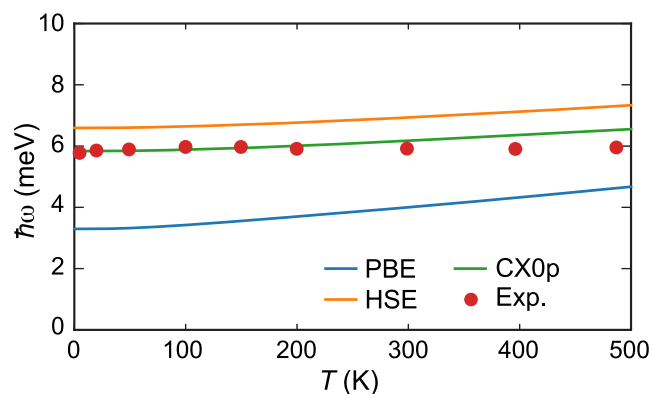


Figure 8. Calculated temperature dependence of the R_{25} phonon mode frequency within the quasi-harmonic approximation. The figure includes a redrawing of the experimental data in Figure 7b.

calculated temperature dependence is determined using the quasi-harmonic approximation⁵⁵ and the results for all three functionals that have positive values for the stiffness parameter κ ; PBE, HSE, and CX0p, are presented. The two hybrid functionals give the best result for frequency at $T = 0$ K, but they also reproduce the weak temperature dependence better compared with PBE. In particular, CX0p gives a very accurate description of the R_{25} phonon mode, both its magnitude and temperature dependence.

4.4. Neutron Compton Scattering Measurements.

The experimental data of the NCS experiment is summarized in Figure 9. Figure 9a shows an example of the mass-resolved Compton profiles in the time-of-flight spectra, where the oxygen peak is well separated from the peaks of the heavier elements Ba and Zr. Here, each peak position, centered along a recoil line, depends on the geometry of the instrument, thus on the source–sample and sample–detector distances, and the scattering angle. For this purpose we show the sum of the spectra from all backscattering detectors after the subtraction of empty-can and closed-circuit-refrigerator backgrounds. Figure 9b shows the sum over all backscattering spectra after the conversion from time-of-flight to the y -space of the oxygen atom, y_{O} , both at $T = 15$ and $T = 300$ K. In this representation,

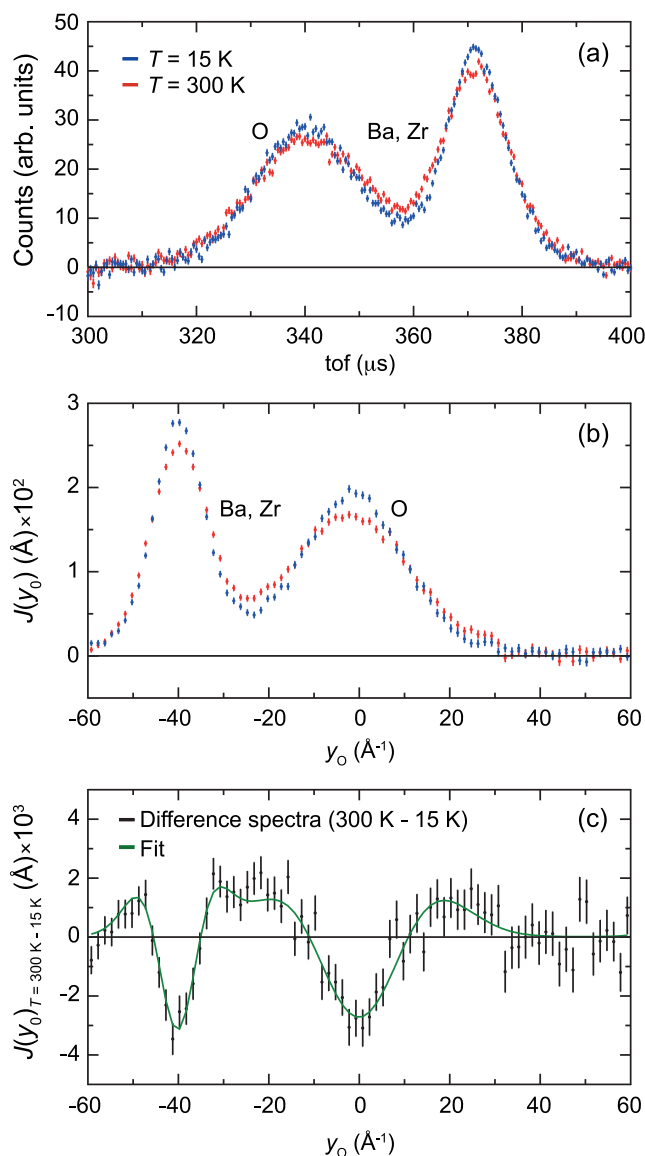


Figure 9. NCS data: (a) sum over all backscattering spectra in time-of-flight after subtraction of the empty-container spectra, (b) sum over all backscattering spectra in the y space of the O atom, and (c) difference of the spectra in panel b together with its best fit.

all oxygen peaks from different detectors share the same position around $y_{\text{O}} \approx 0 \text{ \AA}^{-1}$, i.e., along the oxygen recoil line, with no dependence upon the instrument geometry. The peak at $y_{\text{O}} \approx -40 \text{ \AA}^{-1}$ is the superposition of NCPs from Ba and Zr, whose masses are too large to be resolved in two separate contributions. This latter peak is treated here as a background, that would not appear in the y_{O} -space if the impulse approximation was completely fulfilled, i.e., for infinite values of Q . The amplitudes of these two peaks are defined by the stoichiometry of the system and the values of the neutron scattering cross sections of each atom. In the following analysis, the ratio of these amplitudes (1.29) was therefore fixed. As a first qualitative result, we note that each NCP is broader at higher temperatures as a result of the Boltzmann population factor.

Recently, it has been shown that the analysis of the difference of NCPs can be directly related to the widths σ_M of an NCP at two different temperatures automatically getting rid

off any multiple scattering contribution or other background signal that is not dependent on the sample.³⁸ In this procedure, the change in temperature of a Gaussian NCP defined by standard deviations σ and $\sigma + \delta$ can be expressed as a Taylor expansion in powers of the ratio δ/σ :

$$\frac{J(y, \sigma + \delta) - J(y, \sigma)}{J(y, \sigma)} \approx \left(\frac{y^2}{\sigma^2} - 1 \right) \frac{\delta}{\sigma} + \dots \quad (4)$$

This model has been fitted to the oxygen NCP and to the effective peak from heavier masses in the difference of spectra in Figure 9c. By doing so, the width of the momentum distribution at $T = 15 \text{ K}$ was found to be $\sigma_{\text{O}} = 9.0 \pm 0.5 \text{ \AA}^{-1}$. This value can be related to the width of the square of the wave function in the real space of $0.056 \pm 0.003 \text{ \AA}$. At $T = 300 \text{ K}$ the width of the momentum distribution has increased to $\sigma_{\text{O}} = 10.7 \pm 0.7 \text{ \AA}^{-1}$.

The momentum distribution is related to the mean kinetic energy for the oxygen atom according to $\langle E_{\text{kin}} \rangle = 3\hbar^2\sigma_{\text{O}}^2/2M$. $\langle E_{\text{kin}} \rangle$ increases from $32 \pm 3 \text{ meV}$ at $T = 15 \text{ K}$ to $45 \pm 6 \text{ meV}$ at $T = 300 \text{ K}$. At $T = 15 \text{ K}$ the kinetic energy is mainly due to the ZPE experienced by the oxygen atom. Using the classical expression, $\langle E_{\text{kin}} \rangle = (3/2)k_{\text{B}}T$, we can associate the isotropic experimental NCS value with an effective temperature T^* affecting the oxygen dynamics. At $T = 15 \text{ K}$, we obtain $T^* = 2\langle E_{\text{kin}} \rangle/3k_{\text{B}} \approx 250 \text{ K}$. The ZPE effect is substantial also for oxygen, and it will affect the dynamics at low temperatures.

4.5. Position and Momentum Distributions. The atomic displacements in real space are extracted from the diffraction data and are represented by the mean squared displacements $\langle u^2 \rangle$. The square root of $\langle u^2 \rangle$, $\sigma_u = \sqrt{\langle u^2 \rangle}$, is a measure of the width of the distribution of the position. The analogous distribution of the momenta is measured in the NCS experiment from which the corresponding mean squared momentum $\langle p^2 \rangle$ and width $\sigma_p = \sqrt{\langle p^2 \rangle}$ can be extracted. The position and momentum distributions give complementary information about the displacements of the atoms, in real and in momentum space, respectively. They are related through the Heisenberg uncertainty relation $\sigma_r\sigma_p \geq \hbar^2/2$, where for a harmonic oscillator at $T = 0 \text{ K}$ the equality holds.

Within the harmonic approximation the mean square displacement projected onto the individual atom i and Cartesian direction α as a function of temperature T can be computed according to⁵⁵

$$\langle u_{i,\alpha}^2 \rangle(T) = \frac{1}{N} \sum_{s\mathbf{q}} \frac{\hbar}{2M_i\omega_{s\mathbf{q}}} \left| e_{s\mathbf{q}}^{i,\alpha} \right|^2 \coth(\hbar\omega_{s\mathbf{q}}/2k_{\text{B}}T) \quad (5)$$

where N is the number of unit cells, M_i is the mass of atom i , $\hbar\omega_{s\mathbf{q}}$ is the eigenfrequency for phonon mode s with wavevector \mathbf{q} , and $e_{s\mathbf{q}}^{i,\alpha}$ is the corresponding eigenvector component. Our results at $T = 0 \text{ K}$ are given in Table 3 and compared with the experimental data at $T = 5 \text{ K}$. We find that the oxygen displacement is very anisotropic. $\langle u_{\text{O}_{11}}^2 \rangle$ corresponds to the displacement of the oxygen atom along the Zr–O–Zr bond direction and is quite small corresponding to a high frequency motion and a stiff bond. $\langle u_{\text{O}_{22}}^2 \rangle$ is double degenerate and describes the motion in the plane perpendicular to the Zr–O–Zr direction. It corresponds to the low-frequency R mode, the tilting type of low-frequency motion of the oxygen octahedra. The mean square displacements for the heavier atoms Ba and

Table 3. Comparison between Experimental and Theoretical Values of the Mean Square Displacement $\langle u^2 \rangle$, the Mean Square Momentum $\langle y^2 \rangle$, and the Mean Square Momentum Averaged over the Directions α , σ_0^2 ^a

	exp	PBE	HSE	CX0p
$\langle u_{O_{11}}^2 \rangle$ (10^{-4} \AA^2)	21(3)	21.5	21.3	20.4
$\langle u_{O_{22}}^2 \rangle$ (10^{-4} \AA^2)	58(2)	50.7	49.0	48.9
$\langle u_{Ba}^2 \rangle$ (10^{-4} \AA^2)	18(2)	14.9	14.1	13.2
$\langle u_{Zr}^2 \rangle$ (10^{-4} \AA^2)	12(2)	9.5	9.8	0.4
$\langle y_{O_{11}}^2 \rangle$ (\AA^{-2})		125.8	131.3	138.9
$\langle y_{O_{22}}^2 \rangle$ (\AA^{-2})		0.8	61.1	61.4
$\langle y_{Ba}^2 \rangle$ (\AA^{-2})		182.4	195.4	205.8
$\langle y_{Zr}^2 \rangle$ (\AA^{-2})		294.9	310.1	322.7
σ_0^2	81(9)	80.4	84.5	87.2

^aThe experimental values for $\langle u^2 \rangle$ are the $T = 5 \text{ K}$ values reprinted from Table 1, and σ_0^2 is the value from the NCS experiment at $T = 15 \text{ K}$.

Zr are isotropic and smaller. The experimental data for $\langle u_{O_{22}}^2 \rangle$, $\langle u_{Ba}^2 \rangle$, and $\langle u_{Zr}^2 \rangle$ are somewhat larger, but by taking the uncertainty in the Rietveld refinement into account, we conclude that the agreement between theory and experiments is very good. The temperature dependence of $\langle u^2 \rangle$ is also computed and compared with the experimental data in Figure 10. All three functionals, PBE, HSE, and CX0p, reproduce the experimental results well, both at low and high temperatures.

In analogy with $\langle u^2 \rangle$, the mean square momentum can be expressed as

$$\begin{aligned} \langle p_{i,\alpha}^2 \rangle(T) &\equiv \hbar^2 \langle y_{i,\alpha}^2 \rangle(T) \\ &= \frac{1}{N} \sum_{sq} \frac{M_i \hbar \omega_{sq}}{2} \left| e_{sq}^{i,\alpha} \right|^2 \coth(\hbar \omega_{sq} / 2k_B T) \end{aligned} \quad (6)$$

It is related to the mean kinetic energy for an atom i through $\langle E_{kin} \rangle = \sum_{\alpha} \hbar^2 \langle y_{i,\alpha}^2 \rangle / 2M_i$. In Table 3 we present our computed data for the various atoms. In this case the relation between larger and smaller values for the oxygen atom becomes reversed with $\langle y_{O_{11}}^2 \rangle$ being larger than $\langle y_{O_{22}}^2 \rangle$, consistent with the Heisenberg uncertainty relation. A stiffer bond gives rise to a higher kinetic energy and smaller atomic displacement in real space.

The more robust observable in the NCS measurements is the mean square momentum averaged over the three directions α

$$\sigma_0^2 \equiv \frac{1}{3} (\langle y_{O_{11}}^2 \rangle + 2 \langle y_{O_{22}}^2 \rangle) \quad (7)$$

The computed data at $T = 0 \text{ K}$ and the measured data at $T = 15 \text{ K}$ for this average are given in Table 3, and the temperature dependence is given in Figure 11. We find very good agreement for the average mean square momentum between measurements and calculations (Figure 11). The PBE gives a slightly better agreement, but generally all functionals are (within error) in agreement with the experimental results. In sum, the agreement between experiments and theory, both for the mean square displacement and mean square momentum, is very satisfactory and gives a consistent picture of the oxygen anisotropic vibrational motion, both at low and high temperatures.

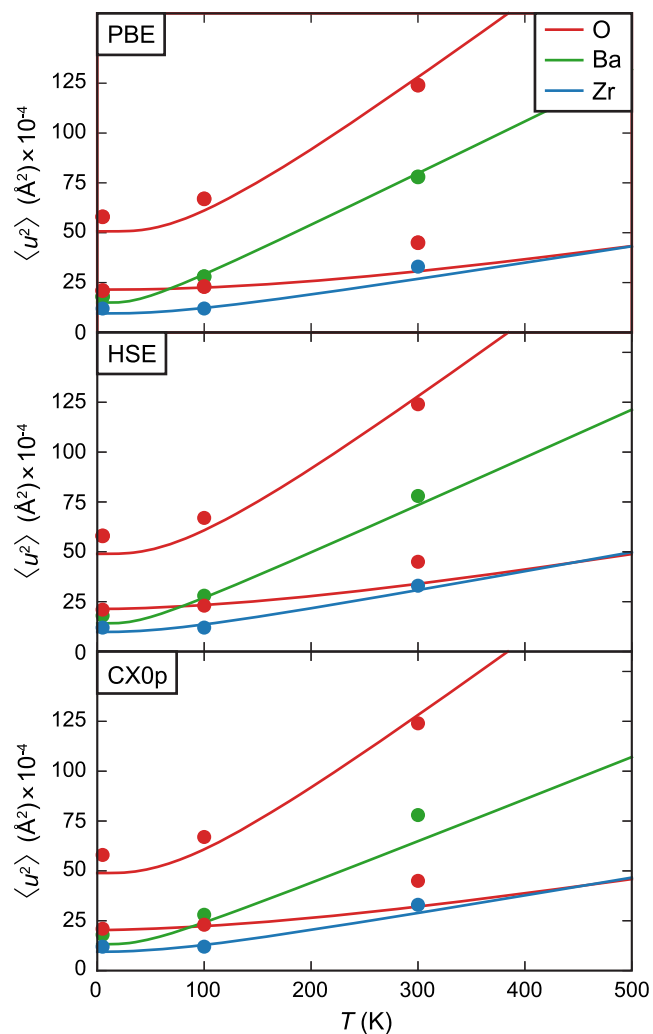


Figure 10. Calculated mean square displacement $\langle u^2 \rangle$ for PBE (top), HSE (middle), and CX0p (bottom). The bullets represent the experimental values from Table 1.

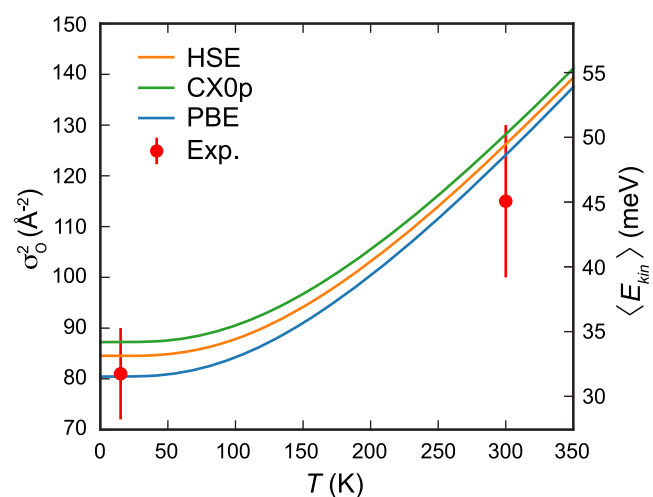


Figure 11. Calculated mean squared momentum averaged over the three directions α (σ_0^2) (left) and mean kinetic energy $\langle E_{kin} \rangle$ (right) as a function of temperature. The bullets represent the experimental values of $\langle E_{kin} \rangle$.

5. SUMMARY AND CONCLUSIONS

We have performed a study of the temperature dependence of the structure and dynamics of BaZrO₃, using a multitechnique approach combining neutron powder diffraction, inelastic neutron scattering, neutron Compton scattering, and first-principles density functional theory calculations.

The density functional theory calculations are performed using six different well-established exchange-correlation functional approximations. The small energy differences between different bulk phases make the theoretical modeling a challenge. While diffraction techniques indicate a cubic structure all the way down to $T = 0$ K, several first-principles phonon calculation studies based on density functional theory indicate an imaginary (unstable) phonon mode due to the appearance of an antiferrodistortive (AFD) transition associated with rigid rotations of ZrO₆ octahedra. We show that only by using hybrid functionals, where some Fock exchange is included, the theoretical modeling leads to predictions fully consistent with experiments.

Specifically, by using the experimental value of the lattice constant, we show that the four functionals LDA, PBE, PBEsol, and CX show a very similar behavior for the AFD mode, i.e. an unstable AFD mode with similar magnitude. The inclusion of truly nonlocal correlations in CX has only a minor effect on the AFD mode. The well-known under- and overestimate of the lattice constant for LDA and PBE, respectively, implies that by using the theoretical lattice constants PBE predicts a stable AFD mode while LDA predicts a highly unstable AFD mode. However, by using the two hybrid functionals, HSE and CX0p, the theory predicts that the cubic phase is stabilized down to $T = 0$ K and the AFD instability is eliminated, both using the experimental and theoretical lattice constants.

The combined analyses of neutron diffraction and Compton scattering data provide complementary information on the atomic displacements in real and momentum space. The diffraction data show that the oxygen displacements are anisotropic, and the data are in very good agreement with the theoretical results, both at low and high temperature. The three different functionals PBE, HSE, and CX0p, which all predict a stable cubic structure, give similar results for the mean squared atomic displacements in real and momentum space and agree within the experimental uncertainties with the neutron Compton data, both at low and high temperatures. This illustrates that neutron Compton scattering is a powerful technique, not only for the momentum distribution for the very light atoms as hydrogen, but also for heavier atoms as oxygen in complex materials.

Further, the analysis of variable temperature inelastic neutron scattering data shows that the low frequency R_{25} mode is quite temperature independent and stable down to at least $T = 5$ K. This is accurately predicted by the two hybrid functionals, HSE, which is based on the constraint-based, semilocal PBE and CX0p based on a current-conserving implementation of the vdW-DF nonlocal-correlation method. Both functionals predict a stable AFD mode but CX0p performs better for the value of the R_{25} -mode frequency and the ZPE-corrected lattice spacing. The result from CX0p compares excellently with the corresponding experimental data. Furthermore, the R_{25} -mode shows a weak temperature dependence, which is predicted by both hybrid functionals. As will be detailed elsewhere, the CX0p functional also performs better than HSE for predictions of thermal expansion and of

extended X-ray absorption fine structure data for BaZrO₃, while the two functionals have matching performances for the dielectric constant of BaZrO₃. The CX0p has the exact same nonlocal correlation as CX and vdW-DF1.⁴⁷ The nonlocal exchange helps set charge transfer effects while the CX nonlocal correlations helps set restoring forces at deformations.⁵⁹ We are pleased to find that CX0p provides an accurate description of the structure and phonons in the BaZrO₃, a nontrivial theoretical modeling task.

To conclude, BaZrO₃ is one of the very few perovskites that stays cubic down to $T = 0$ K. To accurately describe the structure and vibrations of BaZrO₃, hybrid functionals should be used. Quantum fluctuations are present but they are *per se* not responsible for the absence of an AFD transition at low temperatures.

AUTHOR INFORMATION

Corresponding Authors

Maths Karlsson – Departments of Chemistry and Chemical Engineering, Chalmers University of Technology, SE-412 96 Göteborg, Sweden; orcid.org/0000-0002-2914-6332; Email: maths.karlsson@chalmers.se

Göran Wahnström – Department of Physics, Chalmers University of Technology, SE-412 96 Göteborg, Sweden; orcid.org/0000-0003-2305-5330; Email: goran.wahnstrom@chalmers.se

Authors

Adrien Perrichon – Departments of Chemistry and Chemical Engineering, Chalmers University of Technology, SE-412 96 Göteborg, Sweden; orcid.org/0000-0003-0520-0469

Erik Jedvik Granhed – Department of Physics, Chalmers University of Technology, SE-412 96 Göteborg, Sweden; orcid.org/0000-0001-9119-9729

Giovanni Romanelli – ISIS facility, STFC Rutherford Appleton Laboratory, Oxfordshire OX11 0QX, United Kingdom; orcid.org/0000-0001-5963-4647

Andrea Piovano – Institut Laue-Langevin, 38000 Grenoble, France; orcid.org/0000-0002-5005-6307

Anders Lindman – Department of Physics, Chalmers University of Technology, SE-412 96 Göteborg, Sweden; orcid.org/0000-0002-1712-008X

Per Hyldgaard – Department of Microtechnology and Nanoscience–MC2, Chalmers University of Technology, SE-412 96 Göteborg, Sweden; orcid.org/0000-0001-5810-8119

Complete contact information is available at: <https://pubs.acs.org/10.1021/acs.chemmater.9b04437>

Notes

The authors declare no competing financial interest.

ACKNOWLEDGMENTS

This research was funded primarily by the Swedish Research Council (Grant No. 2010-3519), the Swedish Energy Agency (Grant No. 36645-1 and No. 45410-1), and the Swedish Foundation for Strategic Research (Grant No. ICA10-0001 and No. ITM17-0324). The work was partially supported within the CNR-STFC Agreement (2014–2020) concerning collaboration in scientific research at the ISIS Pulsed Neutron and Muon source. We also acknowledge the Rutherford Appleton Laboratory and the Institut Laue-Langevin for access to neutron beam facilities. Andrew Seel is thanked for

assistance during the NCS experiment. The calculations were performed on resources provided by the Swedish National Infrastructure for Computing (SNIC).

REFERENCES

- (1) Kreuer, K. D. Proton-Conducting Oxides. *Annu. Rev. Mater. Res.* **2003**, *33*, 333–359.
- (2) Lone, I. H.; Aslam, J.; Radwan, N. R. E.; Bashal, A. H.; Ajlouni, A. F. A.; Akhter, A. Multiferroic ABO₃ Transition Metal Oxides: a Rare Interaction of Ferroelectricity and Magnetism. *Nanoscale Res. Lett.* **2019**, *14*, 142.
- (3) Uchino, K. Glory of Piezoelectric Perovskites. *Sci. Technol. Adv. Mater.* **2015**, *16*, 046001.
- (4) Zhong, W.; Au, C.-T.; Du, Y.-W. Review of Magnetocaloric Effect in Perovskite-Type Oxides. *Chin. Phys. B* **2013**, *22*, 57501.
- (5) Song, Z.; Zhao, J.; Liu, Q. Luminescent Perovskites: Recent Advances in Theory and Experiments. *Inorg. Chem. Front.* **2019**, *6*, 2969–3011.
- (6) Bae, K.; Young Jang, D.; Jong Choi, H.; Kim, D.; Hong, J.; Kim, B.-K.; Lee, J.-H.; Son, J.-W. S.; Shim, J. H. Demonstrating the Potential of Yttrium-Doped Barium Zirconate Electrolyte for High-Performance Fuel Cells. *Nat. Commun.* **2017**, *8*, 14553.
- (7) Duan, C.; Tong, J.; Shang, M.; Nikodemski, S.; Sanders, M.; Ricote, S.; Almansoori, A.; O'Hayre, R. Readily Processed Protonic Ceramic Fuel Cells with High Performance at Low Temperatures. *Science* **2015**, *349*, 1321–1326.
- (8) Duan, C.; Kee, R.; Zhu, H.; Sullivan, N.; Shu, L.; Bian, L.; Jennings, D.; O'Hayre, R. Highly Efficient Reversible Protonic Ceramic Electrochemical Cells for Power Generation and Fuel Production. *Nature Energy* **2019**, *4*, 230–240.
- (9) Choi, S.; Kucharczyk, C. J.; Liang, Y.; Zhang, X.; Takeuchi, I.; Ji, H.-I.; Haile, S. M. Exceptional Power Density and Stability at Intermediate Temperatures in Protonic Ceramic Fuel Cells. *Nature Energy* **2018**, *3*, 202–210.
- (10) Duan, C.; Kee, R. J.; Zhu, H.; Karakaya, C.; Chen, Y.; Ricote, S.; Jarry, A.; Crumlin, E. J.; Hook, D.; Braun, R.; Sullivan, N. P.; O'Hayre, R. Highly Durable, Coking and Sulfur Tolerant, Fuel-Flexible Protonic Ceramic Fuel Cells. *Nature* **2018**, *557*, 217–222.
- (11) Morejudo, S. H.; Zanón, R.; Escolástico, S.; Yuste-Tirados, I.; Malerød-Fjeld, H.; Vestre, P. K.; Coors, W. G.; Martinez, A.; Norby, T.; Serra, J. M.; Kjøseth, C. Direct Conversion of Methane to Aromatics in a Catalytic Co-Ionic Membrane Reactor. *Science* **2016**, *353*, 563–566.
- (12) Malerød-Fjeld, H.; Clark, D.; Yuste-Tirados, I.; Zanón, R.; Catalán-Martínez, D.; Beeaff, D.; Morejudo, S. H.; Vestre, P. K.; Norby, T.; Haugsrud, R.; Serra, J. M.; Kjøseth, C. Thermo-Electrochemical Production of Compressed Hydrogen from Methane with Near-Zero Energy Loss. *Nature Energy* **2017**, *2*, 923–931.
- (13) Münch, W.; Seifert, G.; Kreuer, K. D.; Maier, J. A Quantum Molecular Dynamics Study of the Cubic Phase of BaTiO₃ and BaZrO₃. *Solid State Ionics* **1997**, *97*, 39–44.
- (14) Björketun, M. E.; Sundell, P. G.; Wahnström, G. Structure and Thermodynamic Stability of Hydrogen Interstitials in BaZrO₃ Perovskite Oxide from Density Functional Calculations. *Faraday Discuss.* **2007**, *134*, 247–265.
- (15) Sundell, P. G.; Björketun, M. E.; Wahnström, G. Density-Functional Calculations of Prefactors and Activation Energies for H Diffusion in BaZrO₃. *Phys. Rev. B: Condens. Matter Mater. Phys.* **2007**, *76*, 094301.
- (16) Zhang, Q.; Wahnström, G.; Björketun, M. E.; Gao, S.; Wang, E. Path Integral Treatment of Proton Transport Processes in BaZrO₃. *Phys. Rev. Lett.* **2008**, *76*, 094301.
- (17) Shannon, R. D. Revised Effective Ionic Radii and Systematic Studies of Interatomic Distances in Halides and Chalcogenides. *Acta Crystallogr., Sect. A: Cryst. Phys., Diffr., Theor. Gen. Crystallogr.* **1976**, *32*, 751–767.
- (18) Redfern, S. A. T. High-Temperature Structural Phase Transitions in Perovskite. *J. Phys.: Condens. Matter* **1996**, *8*, 8267–8275.
- (19) Lytle, F. W. X-Ray Diffractometry of Low-Temperature Phase Transformations in Strontium Titanate. *J. Appl. Phys.* **1964**, *35*, 2212–2215.
- (20) Akbarzadeh, A. R.; Kornev, I.; Malibert, C.; Bellaiche, L.; Kiat, J. M. Combined Theoretical and Experimental Study of the Low-Temperature Properties of BaZrO₃. *Phys. Rev. B: Condens. Matter Mater. Phys.* **2005**, *72*, 205104.
- (21) Zhong, W.; Vanderbilt, D. Competing Structural Instabilities in Cubic Perovskites. *Phys. Rev. Lett.* **1995**, *74*, 2587–2590.
- (22) Bennett, J. W.; Grinberg, I.; Rappe, A. M. Effect of Symmetry Lowering on the Dielectric Response of BaZrO₃. *Phys. Rev. B: Condens. Matter Mater. Phys.* **2006**, *73*, 180102.
- (23) Lebedev, A. I.; Sluchinskaya, I. A. Structural Instability in BaZrO₃ Crystals: Calculations and Experiment. *Phys. Solid State* **2013**, *55*, 1941–1945.
- (24) Bilić, A.; Gale, J. D. Ground State Structure of BaZrO₃: A Comparative First-Principles Study. *Phys. Rev. B: Condens. Matter Mater. Phys.* **2009**, *79*, 174107.
- (25) Chen, P.; Grisolia, M. N.; Zhao, H. J.; González-Vázquez, O. E.; Bellaiche, L.; Bibes, M.; Liu, B.-G.; Iñiguez, J. Energetics of Oxygen-Octahedra Rotations in Perovskite Oxides from First Principles. *Phys. Rev. B: Condens. Matter Mater. Phys.* **2018**, *97*, 024113.
- (26) Amoroso, D.; Cano, A.; Ghosez, P. First-Principles Study of (Ba, Ca)TiO₃ and Ba(Ti, Zr)O₃ Solid Solutions. *Phys. Rev. B: Condens. Matter Mater. Phys.* **2018**, *97*, 174108.
- (27) Bjørheim, T. S.; Kotomin, E. A.; Maier, J. Hydration Entropy of BaZrO₃ from First Principles Phonon Calculations. *J. Mater. Chem. A* **2015**, *3*, 7639–7648.
- (28) Evarestov, R. A. Hybrid Density Functional Theory LCAO Calculations on Phonons in Ba(Ti,Zr,Hf)₃. *Phys. Rev. B: Condens. Matter Mater. Phys.* **2011**, *83*, 014105.
- (29) Zhong, W.; Vanderbilt, D. Effect of Quantum Fluctuations on Structural Phase Transitions in SrTiO₃ and BaTiO₃. *Phys. Rev. B: Condens. Matter Mater. Phys.* **1996**, *53*, 5047–5050.
- (30) Giannici, F.; Shirpour, M.; Longo, A.; Martorana, A.; Merkle, R.; Maier, J. Long-Range and Short-Range Structure of Proton-Conducting Y:BaZrO₃. *Chem. Mater.* **2011**, *23*, 2994–3002.
- (31) Toulouse, C.; Amoroso, D.; Xin, C.; Veber, P.; Hatnean, M. C.; Balakrishnan, G.; Maglione, M.; Ghosez, P.; Kreisel, J.; Guennou, M. Lattice Dynamics and Raman spectrum of BaZrO₃ Single Crystals. *Phys. Rev. B: Condens. Matter Mater. Phys.* **2019**, *100*, 134102.
- (32) Rodríguez-Carvajal, J. Recent Advances in Magnetic Structure Determination by Neutron Powder Diffraction. *Phys. B* **1993**, *192*, 55–69.
- (33) Mayers, J.; Reiter, G. The VESUVIO Electron Volt Neutron Spectrometer. *Meas. Sci. Technol.* **2012**, *23*, 045902.
- (34) Andreani, C.; Colognesi, D.; Degiorgi, E.; Filabozzi, A.; Nardone, M.; Pace, E.; Pietropaolo, A.; Senesi, R. Double Difference Method in Deep Inelastic Neutron Scattering on the VESUVIO Spectrometer. *Nucl. Instrum. Methods Phys. Res., Sect. A* **2003**, *497*, 535–549.
- (35) Andreani, C.; Krzystyniak, M.; Romanelli, G.; Senesi, R.; Fernandez-Alonso, F. Electron-Volt Neutron Spectroscopy: Beyond Fundamental Systems. *Adv. Phys.* **2017**, *66*, 1–73.
- (36) Ivanov, G. K.; Sayasov, Y. S. Theory of the Vibrational Excitation of a Molecule in the Impulse Approximation. *Soviet Physics Doklady* **1964**, *9*, 171.
- (37) Romanelli, G.; Ceriotti, M.; Manolopoulos, D. E.; Pantalei, C.; Senesi, R.; Andreani, C. Direct Measurement of Competing Quantum Effects on the Kinetic Energy of Heavy Water upon Melting. *J. Phys. Chem. Lett.* **2013**, *4*, 3251–3256.
- (38) Romanelli, G.; Krzystyniak, M. On the Line-Shape Analysis of Compton Profiles and its Application to Neutron Scattering. *Nucl. Instrum. Methods Phys. Res., Sect. A* **2016**, *819*, 84–88.
- (39) Blöchl, P. E. Projector Augmented-Wave Method. *Phys. Rev. B: Condens. Matter Mater. Phys.* **1994**, *50*, 17953–17979.

(40) Kresse, G.; Joubert, D. From Ultrasoft Pseudopotentials to the Projector Augmented-Wave Method. *Phys. Rev. B: Condens. Matter Mater. Phys.* **1999**, *59*, 1758–1775.

(41) Kresse, G.; Furthmüller, J. Efficiency of Ab-Initio Total Energy Calculations for Metals and Semiconductors using a Plane-Wave Basis Set. *Comput. Mater. Sci.* **1996**, *6*, 15–50.

(42) Kresse, G.; Furthmüller, J. Efficient Iterative Schemes for Ab Initio Total-Energy Calculations Using a Plane-Wave Basis Set. *Phys. Rev. B: Condens. Matter Mater. Phys.* **1996**, *54*, 11169–11186.

(43) Perdew, J. P.; Burke, K.; Ernzerhof, M. Generalized Gradient Approximation Made Simple. *Phys. Rev. Lett.* **1996**, *77*, 3865–3868.

(44) Perdew, J. P.; Ruzsinszky, A.; Csonka, G. I.; Vydrov, O. A.; Scuseria, G. E.; Constantin, L. A.; Zhou, X.; Burke, K. Restoring the Density-Gradient Expansion for Exchange in Solids and Surfaces. *Phys. Rev. Lett.* **2008**, *100*, 136406.

(45) Berland, K.; Hyldgaard, P. Exchange Functional that Tests the Robustness of the Plasmon Description of the van der Waals Density Functional. *Phys. Rev. B: Condens. Matter Mater. Phys.* **2014**, *89*, 035412.

(46) Berland, K.; Arter, C. A.; Cooper, V. R.; Lee, K.; Lundqvist, B. I.; Schröder, E.; Thonhauser, T.; Hyldgaard, P. van der Waals Density Functionals built upon the Electron-Gas tradition: Facing the Challenge of Competing Interactions. *J. Chem. Phys.* **2014**, *140*, 18A539.

(47) Dion, M.; Rydberg, H.; Schröder, E.; Langreth, D. C.; Lundqvist, B. I. Van der Waals Density Functional for General Geometries. *Phys. Rev. Lett.* **2004**, *92*, 246401.

(48) Hyldgaard, P.; Berland, K.; Schröder, E. Interpretation of van der Waals Density Functionals. *Phys. Rev. B: Condens. Matter Mater. Phys.* **2014**, *90*, 075148.

(49) Berland, K.; Cooper, V. R.; Lee, K.; Schröder, E.; Thonhauser, T.; Hyldgaard, P.; Lundqvist, B. I. van der Waals Forces in Density Functional Theory: a Review of the vdW-DF Method. *Rep. Prog. Phys.* **2015**, *78*, 066501.

(50) Jiao, Y.; Schröder, E.; Hyldgaard, P. Extent of Fock-Exchange Mixing for a Hybrid van der Waals Density Functional? *J. Chem. Phys.* **2018**, *148*, 194115.

(51) Berland, K.; Jiao, Y.; Lee, J.-H.; Rangel, T.; Neaton, J. B.; Hyldgaard, P. Assessment of two Hybrid van der Waals Density Functionals for Covalent and Non-Covalent Binding of Molecules. *J. Chem. Phys.* **2017**, *146*, 234106.

(52) Jiao, Y.; Schröder, E.; Hyldgaard, P. Signatures of van der Waals Binding: A Coupling-Constant Scaling Analysis. *Phys. Rev. B: Condens. Matter Mater. Phys.* **2018**, *97*, 085115.

(53) Heyd, J.; Scuseria, G. E.; Ernzerhof, M. Hybrid Functionals based on a Screened Coulomb Potential. *J. Chem. Phys.* **2003**, *118*, 8207–8215.

(54) Heyd, J.; Scuseria, G. E.; Ernzerhof, M. Erratum: Hybrid Functionals based on a Screened Coulomb Potential [*J. Chem. Phys.* **118**, 8207 (2003)]. *J. Chem. Phys.* **2006**, *124*, 219906.

(55) Togo, A.; Tanaka, I. First Principles Phonon Calculations in Materials Science. *Scr. Mater.* **2015**, *108*, 1–5.

(56) Perrichon, A. *PowderTAS: Neutron Scattering Cross-sections for Powder Samples*; 2019; DOI: 10.5281/zenodo.3371370.

(57) Zhong, W.; Vanderbilt, D.; Rabe, K. M. Phase Transitions in BaTiO₃ from First Principles. *Phys. Rev. Lett.* **1994**, *73*, 1861–1864.

(58) Yang, X.; Li, Q.; Liu, R.; Liu, B.; Zhang, H.; Jiang, S.; Liu, J.; Zou, B.; Cui, T.; Liu, B. Structural Phase transition of BaZrO₃ under High Pressure. *J. Appl. Phys.* **2014**, *115*, 124907.

(59) Erhart, P.; Hyldgaard, P.; Lindroth, D. Microscopic Origin of Thermal Conductivity Reduction in Disordered van der Waals Solids. *Chem. Mater.* **2015**, *27*, 5511–5518.